

In-situ monitoring of a laser metal deposition (LMD) process: comparison of MWIR, SWIR and high-speed NIR thermography

Simon J. Altenburg , Anne StraÙe , Andrey Gumenyuk & Christiane Maierhofer

To cite this article: Simon J. Altenburg , Anne StraÙe , Andrey Gumenyuk & Christiane Maierhofer (2020): In-situ monitoring of a laser metal deposition (LMD) process: comparison of MWIR, SWIR and high-speed NIR thermography, Quantitative InfraRed Thermography Journal, DOI: [10.1080/17686733.2020.1829889](https://doi.org/10.1080/17686733.2020.1829889)

To link to this article: <https://doi.org/10.1080/17686733.2020.1829889>



© 2020 The Author(s). Published by Informa UK Limited, trading as Taylor & Francis Group.



[View supplementary material](#)



Published online: 04 Nov 2020.



[Submit your article to this journal](#)



[View related articles](#)



[View Crossmark data](#)

In-situ monitoring of a laser metal deposition (LMD) process: comparison of MWIR, SWIR and high-speed NIR thermography

Simon J. Altenburg ^a, Anne StraÙe ^b, Andrey Gumenyuk ^b
and Christiane Maierhofer ^a

^aBundesanstalt Für Materialforschung Und -prüfung, department 8.7: Thermographic Methods, Unter den Eichen 87, Berlin, Germany; ^bBundesanstalt Für Materialforschung Und -prüfung, department 9.3: Welding Technology, Unter den Eichen 87, Berlin, Germany

ABSTRACT

Additive manufacturing offers a range of novel applications. However, the manufacturing process is complex and the production of almost defect-free parts with high reliability and durability is still a challenge. Thermography is a valuable tool for process surveillance, especially in metal additive manufacturing processes. The high process temperatures allow one to use cameras usually operating in the visible spectral range. Here, we compare the results of measurements during the manufacturing process of a commercial laser metal deposition setup using a mid wavelength infrared camera with those from a short wavelength infrared camera and those from a visual spectrum high-speed camera with band pass filter in the near infrared range.

ARTICLE HISTORY

Received 3 June 2020
Accepted 20 September 2020


KEYWORDS

additive manufacturing;
thermography; LMD; SWIR;
MWIR; NIR; process
monitoring; metal

1. Introduction

Additive manufacturing (AM) offers a range of novel applications, from the production of parts with a complex geometry that cannot be built by classical manufacturing in a single piece to highly individualised production on end-customer demand. However, the manufacturing process is complex and the production of almost defect-free parts with high reliability and durability is still a challenge [1]. Depending on the AM method (e. g. laser metal deposition (LMD), laser powder bed fusion (L-PBF), electron beam powder bed fusion (E-PBF), wire arc additive manufacturing (WAAM)), different types of defects and inhomogeneities might occur [1,2]. LMD is used if larger deposition rates and only a limited complexity of the part geometry is required. It is applied as laser cladding for coatings, as a repair process for worn pieces as well as for the creation of 3D functional components. In this process, a laser generates a small melt pool on the surface of the substrate and the metal powder, which is dispensed by a powder feeder, is injected into this melt pool by a stream of inert carrier gas. A relative movement between work piece and LMD-nozzle is used for the build-up of the parts. Typical defects and inhomogeneities in LMD coatings and

CONTACT Simon J. Altenburg  Simon.Altenburg@bam.de  Bundesanstalt Für Materialforschung Und -prüfung, Berlin 12205, Germany

 Supplemental data for this article can be accessed [here](#).

© 2020 The Author(s). Published by Informa UK Limited, trading as Taylor & Francis Group.

This is an Open Access article distributed under the terms of the Creative Commons Attribution-NonCommercial-NoDerivatives License (<http://creativecommons.org/licenses/by-nc-nd/4.0/>), which permits non-commercial re-use, distribution, and reproduction in any medium, provided the original work is properly cited, and is not altered, transformed, or built upon in any way.

parts are an enhanced porosity due to gas pores and/or shrinkage pores, lack of fusion, cracks inside the volume and/or at the surface, deviations from the original geometry, higher surface roughness than expected, inhomogeneous microstructures, inclusions of contaminations, and internal stress [1,3,4]. These inhomogeneities might lead to reduced mechanical properties and shorter lifetimes of the built components. Most of these defects can be attributed to the manufacturing process itself, which therefore is usually monitored by laser irradiation and camera based systems [2,5]. In addition to the surveillance of process parameters, different in-process NDT techniques can be implemented. Thermography has been proven to be a valuable tool for melt pool control, especially in metal AM processes [1,2,6,7]. It allows the determination of the melt pool temperature, its dimensions and dynamics as well as cooling rates and spatial temperature gradients. However, there are certain hurdles to be overcome to assure a reliable thermographic process surveillance in metal AM. First, the complexity of the emissivity (temperature, angle, aggregate state, wavelength, and composition dependency) poses a challenge [8]. Second, the accessibility of the process itself may be limited due to constraints defined by the production setup. As for all laser-based methods, laser safety has to be ensured. Despite these challenges, the high process temperatures of more than 2500 K (depending on the used material) allow one to use cameras usually operating in the short wavelength infrared (SWIR) and visible (VIS) spectral range, in addition to mid wavelength infrared (MWIR) and long wavelength infrared (LWIR) cameras, to monitor the process, since a significant amount of thermal radiation is emitted in the infrared and the visual spectrum range. A calibration of a VIS camera for temperature measurement is possible (VIS thermography) [9]. To avoid disturbing influences from emissions of the welding plasma, a wavelength limitation of the detected radiation to a narrower band in the near infrared (NIR) is desirable and can be realised by a band pass filter.

Here, we present results of experiments for temperature monitoring during an LMD process, using currently available hardware, that were performed in order to gather experience for the choice of a process-optimised camera system. To this end, experiments using stationary cameras operating in the MWIR and the VIS range (limited by a narrow band pass filter in the NIR) were executed. Additionally, we compare those results to results from measurements obtained by using a camera operating in the SWIR range, that was acquired based on the findings of the former experiments. Therefore, for the first time, VIS, SWIR, and MWIR cameras are directly compared to each other to decide which currently commercially available system is best suited for in-situ monitoring of the LMD process.¹ In addition, options for optimised systems are discussed concerning the needs for spatial, temporal and thermal resolution as well as for thermal range.

An approximate temperature calibration of the cameras, using the grey body approximation and the solidification temperature as input, was performed. It is shown that the VIS camera has a very limited measurable temperature range, compared to the MWIR camera, while the temperature dynamic of the SWIR camera was intermediate. On the other hand, the MWIR camera detects strong reflections from the build plate and spatial inhomogeneities in the heated area that are most likely caused by inhomogeneities of the emissivity. The VIS camera did not show these effects. As expected, the SWIR-camera combines advantages of the MWIR and the VIS cameras.

In [Table 1](#), all abbreviations used in this article are summarised.

Table 1. List of abbreviations.

Abbreviation	Full length
AM	Additive Manufacturing
D.V.	Digital values
LMD	Laser Metal Deposition
L-PBF	Laser Powder Bed Fusion
LWIR	Long wavelength infrared range (8.0 to 14.0 μm)
MWIR	Mid wavelength infrared range (2.0 to 5.0 μm)
NDT	Non-destructive testing
NIR	Near Infrared
SWIR	Short wavelength infrared range (0.8 to 2.0 μm)
VIS	Visual wavelength range (here: 0.4 to 1.0 μm)
WAAM	Wire Arc Additive Manufacturing

2. Experimental details

In this section, we describe the experimental setup.

2.1. AM setup

The AM setup, used for the experiments, is a commercial laser metal deposition cell of the manufacturer Trumpf (Trumpf GmbH + Co. KG, Ditzingen, Germany), type TruLaser Cell 3000. It is coupled with a 16 kW Yb:YAG TruDisk 16,002 – disk laser (Trumpf) with a wavelength of 1030 nm. The laser head can be moved in x-, y- and z-direction and tilted to both sides in a maximum angle of 135°. The volume of the build space is 800 mm x 600 mm x 400 mm. The powder deposition onto the substrate is achieved with an integrated three-jet SO16-powder nozzle, having a working distance of 16 mm measured from the nozzle edge. The three powder tubes are arranged around the laser beam coaxially at 120° angles, see [Figure 1](#). The powder jets are focussed in a spot of approximately 3.5 mm diameter at this distance. The optical head is equipped with a flexible collimation unit allowing to adjust the focus diameter of the laser beam in the range between approximately 0.4 mm and 3.8 mm at the working plane.

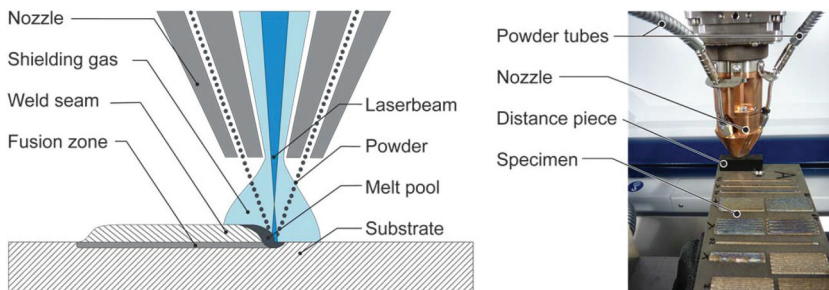


Figure 1. Left: LMD process (schematic), right: Photograph of the SO16-nozzle with 16 mm distance piece.

2.2. Thermographic setup

Three different cameras, operating in the MWIR, the SWIR and the VIS range, were used to monitor the thermal radiation emitted during the building process. Regarding the comparison between MWIR and the VIS camera, the measurements were performed on different occasions in a comparable setup with similar process parameters. The MWIR (VIS) camera was mounted at a fixed position in the build chamber at a distance of 40 cm (30 cm) between front most lens and the focal point of the laser. The angle between the optical axis of the camera and the surface normal of the base plate was approximately 60°. Photographs of the experimental setup are shown in [Figure 2](#), left and middle. For the comparison between MWIR and SWIR camera, the data were acquired simultaneously on a third occasion and with different material and process parameters. Here, the distance between the front most lens (or filter in case of the SWIR camera) and the focal point of the laser was 35.5 cm and 39 cm for the MWIR and the SWIR camera, respectively. The angle between the optical axis of the camera and the surface normal of the base plate was approximately 40°. The side-view of the experiment was as shown in [Figure 2](#), right, but with the SWIR-camera mounted behind the MWIR camera. The superimposed image of the SWIR camera was taken from the manufacturers datasheet and does not show the actually used objective and filters.

The used MWIR camera of type InfraTec ImageIR 8300 (InfraTec GmbH Infrarotsensorik und Messtechnik, Dresden, Germany) is sensitive in the spectral range between 2 μm and 5.5 μm (cooled InSb-focal-plane-array) and is temperature calibrated in the range between 773 K and 1473 K (black body) using an absorptive filter within the camera. The integration time was set to 47 μs and the bit resolution was 14 bit. In the first set of experiments (comparison MWIR-VIS), it was operated at a frequency of 800 Hz in sub-frame-mode (320 \times 156 pixels) with a pixel resolution of 240 μm . In the second set of experiments (comparison MWIR-SWIR), it was operated at a frequency of 500 Hz in subframe-mode (240 \times 176 pixels) and at a frequency of 100 Hz in full frame-mode (640 \times 512 pixels) with a pixel resolution of 260 μm .

The VIS camera of type Fastcam SA4 (Photron Inc., San Diego, CA, USA, high speed camera with 32 GB internal memory) was equipped with a narrow band pass filter, limiting the detected light to a wavelength range between 807 nm and 817 nm. It was operated at

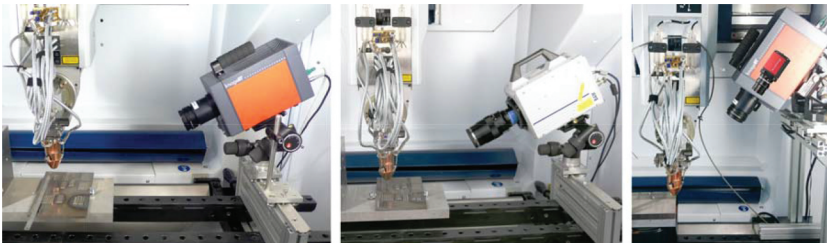


Figure 2. Photographs of the experimental setup. Left: MWIR setup, middle: VIS setup, right: SWIR setup (the small SWIR camera was actually behind the MWIR camera, size and position illustrated by montage of image of the SWIR camera from manufacturers datasheet, not including the used objective and filters), together with MWIR setup. Please note that the angle of the optical axes of the MWIR and VIS camera used in the first experimental run related to the surface normal was 60°, while it was only 40° for the MWIR and SWIR camera in the second experimental run.

a frequency of 10 kHz at a subframe resolution of 768×240 pixels with a pixel resolution of $48 \mu\text{m}$. An integration time of $100 \mu\text{s}$ was set. To reduce the amount of data, the possible bit resolution of 12 bit was reduced to 8 bit.

The used SWIR camera of type Allied Vision Goldeye CL-033 TEC1 (Allied Vision Technologies GmbH, Stadroda, Germany) is sensitive in the spectral range between $0.9 \mu\text{m}$ and $1.7 \mu\text{m}$ (temperature stabilised InGaAs-focal-plane-array) and was operated with a band pass filter with a central wavelength of 1550 nm and a width of 25 nm as well as with neutral density filters (ND1.0 + ND1.5) and an additional long pass filter with a cut on wavelength of 1175 nm , to completely block the welding laser. The camera is not temperature calibrated and was operated at a frequency of 500 Hz in subframe-mode (640×171 pixels) with a pixel resolution of $125 \mu\text{m}$. The integration time was set to 2 ms and the bit resolution was 14 bit.

The specifications and selected measurement parameters of all cameras are summarised in [Table 2](#).

2.3. Build parameters

In the first experiments comparing MWIR and VIS, the following build parameters were used: The build plate was made of polished carbon steel and the powder material was AISI 2205 duplex stainless steel with an average diameter range from $53 \mu\text{m}$ to $125 \mu\text{m}$ and a powder mass flow of 17 g/min . The laser power P was set to 1.7 kW with a Gaussian beam profile and a beam diameter d of 3 mm . The welding velocity v was set to 13.3 mm/s . The powder carrier gas was helium with a flowrate of 4 l/min and the shielding gas was argon with a flowrate of 10 l/min . The build geometry was a stack of single lines (i.e. a wall) of 45 mm (25 mm) length consisting of up to 9 layers (3 layers) for the MWIR (VIS) camera, which were welded unidirectionally without pauses between the layers.

In the second experimental run comparing MWIR and SWIR cameras, which were operated simultaneously, the following build parameters were used: The build plate was made of non-polished (as delivered) 316 L steel and the powder material was 316 L-Si steel with an average diameter range from $44 \mu\text{m}$ to $106 \mu\text{m}$ and a mass flow density of 17 g/min . The laser power was set to 1.2 kW with a Gaussian beam profile and a beam diameter of 2.4 mm . The welding velocity was set to 21.7 mm/s . The powder carrier gas was argon with a flowrate of 4 l/min and the shielding gas was argon with a flowrate of 10 l/min . The build geometry was a stack of single lines (wall) of 70 mm length consisting of up to 10 layers, which were welded unidirectionally without pauses between the layers.

The build parameters of the two experimental runs are summarised in [Table 3](#). Here, the areal energy density U can be calculated from the emitted laser power P , the laser spot diameter d and the welding velocity v by Equation 1:

$$U = \frac{P}{d \cdot v} \quad (1)$$

Table 2. Specifications of the applied MWIR, SWIR and VIS cameras*.

Name	Type of detector	Wave length in μm	Filter	Bit resolution	Maximum valid intensity, before calibration	Integration time in μs	Frame rate in kHz	Pixels	Spatial resolution per pixel in μm
MWIR, InfraTec ImageIR 8300a	Cooled InSb	2 to 5.5	-	14	1473 K	47	0.8 (0.5, 0.1)	320 x 156 (240 x 176, 640 x 512)	240 (260)
SWIR Allied Vision Goldeye CL 033 TEC1	Temperature stabilized InGaAs	0.9 to 1.7	1.525 μm to 1.575 μm , ND1.0, ND 1.5 and >1.175 μm	14	16,383 D.V.	2000	0.5	640 x 171	125
VIS Photon Fastcam SA4	CMOS	0.4 to 1.0	0.807 μm to 0.817 μm	12 (8 were used)	4095 D.V. (255 D.V. with used 8 bit resolution)	100	10	768 x 240	48

* Measurement parameters of the MWIR camera of the first experimental run (combination with VIS camera) are shown without brackets, those from the second experimental run (combination with SWIR camera) with brackets, italic letters denote values for single measurement in full-frame mode.

Table 3. Build parameters of the two experimental runs.

Parameter	First experimental run	Second experimental run
Powder Material	AISI 2205 duplex stainless steel	316 L stainless steel
Build plate material	Carbon steel, polished	316 L stainless steel, as delivered
Build plate thickness	6 mm	20 mm
Laser power P	1.7 kW	1.2 kW
Laser spot diameter d	3 mm	2.4 mm
Welding velocity v	13.3 mm/s	21.7 mm/s
Areal energy density U	43 J/mm ²	23 J/mm ²
Mass flow density	17 g/min	17 g/min

3. Experimental results and discussion

3.1. First experimental run, comparison between MWIR and VIS cameras

Selected thermograms from the build process (building direction from right to left) for different layers recorded with the MWIR camera are shown in Figure 3, together with a photograph of the built structure. Since the camera is calibrated assuming a perfect black body radiator, an assumption that is not met here, the given temperatures are only apparent. Firstly, it can be seen that the size of the heated zone increases with the layer number (Figure 3(a–c)), which can be explained by the decrease in heat dissipation to the build plate with an increase in part height and heat accumulation. Secondly, reflections from the base plate and shadowing of these reflections by other built structures on the build plate become visible in Figure 3(b) and more clearly in Figure 3(c) (compare to photograph in Figure 3(d)). Thirdly, the intensity distribution within the melt pool appears

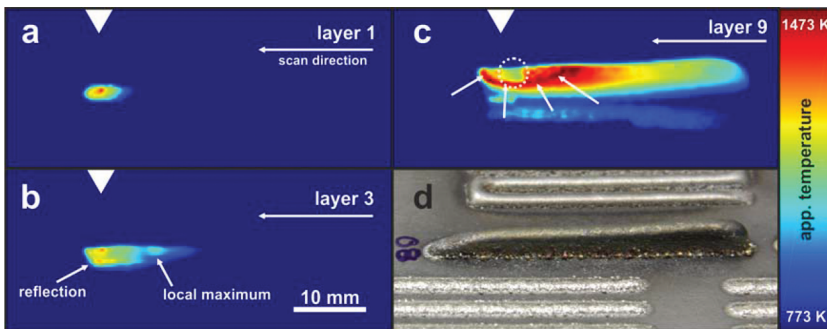


Figure 3. (a–c): Thermograms recorded with the MWIR camera during the build of the indicated layers. The approximate horizontal position of the nozzle is indicated by a white triangle. (a): First layer, the melt pool appears homogeneous with a well-defined hotspot at the centre. Thermogram at 2.7 s of 3.4 s build duration of the layer (starting at 0 s), corresponding to a time of 01 min 25 s in supplementary video 1. (b): Third layer, a second hot spot marked ‘reflection’ is observable as well as a ‘local maximum’. Thermogram at 2.5 s of 3.4 s build duration of the layer, corresponding to a time of 05 min 43 s in supplementary video 1. (c): Ninth layer, a complicated intensity distribution is observable. There is a high intensity rim around the melt pool (arrows) and an area with a lower temperature appears at the position of the melt pool (dashed circle). Reflections from the build plate and shadowing by previously built structures can be seen (compare to d). Thermogram at 2.5 s of 3.4 s build duration of the layer, corresponding to a time of 18 min 58 s in supplementary video 1. (d): Photograph of the built structure (total of nine layers) from a similar angle. The structures shadowing in c can be identified. The scale of the apparent temperature on the right is valid for all thermograms.

only in [Figure 3\(a\)](#) (layer 1) as one might expect (a maximum at the centre with a decay in all directions). In [Figure 3\(b\)](#), a second maximum below the most intense one can be seen, that is probably caused by reflections of radiation from the wall at the build plate. However, another local maximum can be seen on the right-hand side, whose origin is not fully understood. One possible explanation that will be further examined in the future is that there is a region of undercooling in the melt pool with still a liquid aggregate state between the two maxima [10]. Another probable cause is a local variation of the emissivity. At the position of the right maximum, solidification has occurred. As the solid surface usually has a higher emissivity than the liquid surface (the solid surface is rougher than the liquid surface), the solid surface appears warmer. Other reasons like oxidation or further impurities could further increase the emissivity in the solid state. In [Figure 3\(c\)](#) (layer 9), the melt pool appears strongly inhomogeneous. In particular, a rim of increased intensity is observable around the melt pool (marked by arrows), which is most likely rather caused by an increased emissivity in this region (slag formation [11]) than by an actual temperature increase. This interpretation is supported by the presence of an apparently cold spot within the molten pool (presumably an area of unoxidised clean molten metal with low emissivity, marked by a dotted circle) and higher maximum apparent temperatures than in the previous layers (1514 K at the rim of the melt pool compared to 1402 K in layer 1 (a) and 1336 K in layer 3 (b), both at the centre of the melt pool), marked by arrows. This is consistent with higher degrees of oxidation in higher layers, which might be caused by accumulation of oxides that stay at the surface of the upmost layer during manufacturing and by the increased area of hot metal due to heat accumulation. This heat accumulation results in a less efficient shielding by the inert gas, which is localised around the welding spot. Further investigations of the oxidation behaviour during the build are planned, e. g., by varying systematically the process parameters [12]. The complex distribution and evolution of the emissivity will be studied in detail by the use of multispectral thermography [13] and temperature emissivity separation algorithms [14] in the future.

[Figure 4](#) shows a comparison of a thermogram of the MWIR camera (same as [Figure 3\(b\)](#), third layer) and an intensity image of the VIS camera, recorded during the build of the third

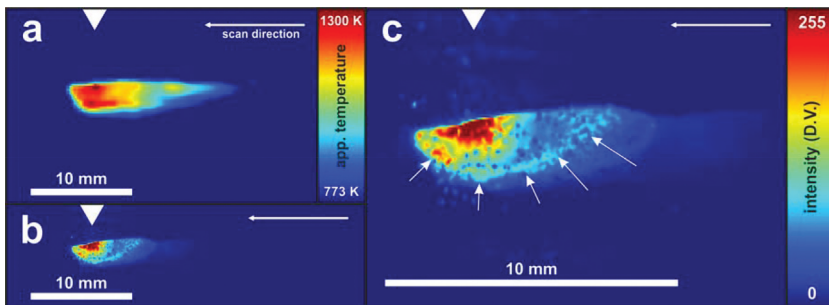


Figure 4. Apparent temperature and intensity images recorded during the build of the third layer of the wall. The approximate horizontal position of the nozzle is indicated by a triangle. (a): Recorded with the MWIR camera (same as [Figure 3\(b\)](#)) with adjusted colour scale. b/c: Recorded with the VIS camera with NIR filter. Thermogram at 1.2 s of 1.9 s build duration of the layer, corresponding to a time of 09 min 27 s in supplementary video 2. (b): Same geometrical scale as a, c: enlarged view. Mainly the melt pool is visible. Shadowing by powder particles and irregular structures within the melt pool can be observed as well as a slight rim of increased intensity around the melt pool (arrows).

layer. Comparing [Figure 4\(a\)](#) (MWIR) and [Figure 4\(b\)](#) (VIS) at the same geometric scale, the most remarkable difference is the different apparent size of the heated zone. This is mainly caused by the limited dynamic temperature range of the VIS camera in combination with the much larger intensity contrast between emitters of different temperatures in the NIR range than in the MWIR range. Using an approximate temperature calibration (see below), the temperature range of the VIS camera is limited to a range of 1300 K to 2000 K, while the MWIR camera can detect the intensity of real temperatures from roughly 800 K to 2300 K in the current example by considering a low emissivity around 0.29 (see below). Thus, the measurement of the VIS camera is limited to the hottest part of the process, which is related to a smaller region in the thermogram. Contrary to the thermogram of the MWIR camera, there are no signs of reflections in the thermogram of the VIS camera. This is expected, as possible reflections of lower intensity are cut off by the detection limit of the VIS camera. In the thermogram of the VIS camera, there is no sign of the additional local maximum on the right-hand side of the melt pool that can be seen in the MWIR image. Either the intensity of this structure is below the detection limit of the camera or the effect leading to this signature is not present at the wavelength of the VIS camera. [Figure 4\(c\)](#) shows an enlarged view of [Figure 4\(b\)](#). Due to the higher spatial resolution of the VIS camera, a lot of details can be observed that are not visible in the MWIR thermogram. Firstly, we can see that there is a small region in the image that is overexposed (dark red), so the dynamic range of the camera is completely used, and the highest intensity values are cut off. Similar to [Figure 3\(c\)](#), there is a rim around the melt pool with an increased intensity (marked by arrows). However, contrary to [Figure 3\(c\)](#), the intensity value of this rim is well below the maximum intensity of the thermogram. From the time series of thermograms of the VIS camera (see supplementary video 2), it can be seen that various small low intensity spots can be attributed to powder particles that fly through the image, shadowing parts of the melt pool. Others of these spots appear to be swimming in the melt pool and dissolve after a certain time. An additional observation from the time series, that is not visible in the single thermogram, is a slight swirling of the melt pool. However, it is unclear whether these details will in fact be useful for purposes of process monitoring. Note that the laser was switched off for a duration of 75 ms (approximately 7 min 27 s to 7 min 57 s in the video 2) to analyse the effect of such a disturbance on the measured signal. However, this analysis is beyond the scope of the current work.

[Figure 5](#) shows the time evolution of the measured signals at single points in space that the laser passes with maximum intensity during the build of the first layer. [Figure 5\(a\)](#) displays the signal of the MWIR camera for a single pixel. Note that the heating duration is approximately 0.23 s, based on the current laser spot diameter and welding velocity. During heating, there is a shoulder in the apparent temperature, probably caused by the melting of the material. It is followed by a maximum (further heating of the melt), followed by a decrease of the apparent temperature, a plateau (caused by the solidification of the melt) and a further decrease. This general shape of the temperature development during the build has previously been reported [15] and allows one to determine an effective emissivity value by using the grey body approximation and adjusting the emissivity in such a way that the temperature of the solidification plateau equals the known solidification temperature of the used material. To this end, we calculated the incident radiance on the camera detector during calibration at the black body $\Phi_{BB}(T_m)$ ($\epsilon = 1$, valid through the vendors calibration) by integrating the Planck equation

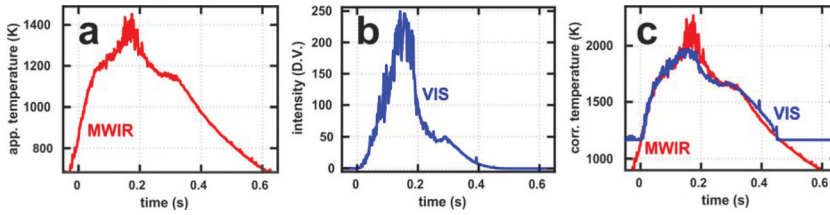


Figure 5. Time evolution of the measured signal at a position that is passed by the laser in the first layer. The time axes were shifted to match. (a): Measured with the MWIR camera (emissivity setting $\epsilon = 1$), single pixel. (b): Measured with the VIS camera and averaged over 5×5 pixel (to match the pixel size of the MWIR camera), using a running average filter of 21 frames. c: Data of a and b after simple calibration procedure (see text).

in the sensitive spectral range of the camera for the temperature T_m , displayed by the camera. The radiance of a grey body is given by

$$\Phi(\epsilon, T) = \epsilon \cdot \Phi_{BB}(T) + (1 - \epsilon) \cdot \Phi_{BB}(T_0) \quad (2)$$

($T_0 = 300$ K: temperature of the surroundings). Assuming a solidification temperature of $T_{s,2205} = 1653$ K (average of liquidus and solidus temperature) for AISI 2205 [16] and setting

$$\Phi(\epsilon_{2205}, T_{s,2205}) = \Phi_{BB}(T_{m,s,2205}) \quad (3)$$

where $T_{m,s,2205}$ is the temperature at the solidification plateau displayed by the camera, yielded an effective emissivity of $\epsilon_{2205} = 0.29$. Thus, as emissivity correction, temperatures T_{corr} that fulfil

$$\Phi(\epsilon_{2205}, T_{corr}) = \Phi_{BB}(T_m) \quad (4)$$

were used. Results of the correction are shown in [Figure 5\(c\)](#). Note that the actual solidification temperature of the material is not known exactly, since the molten material is a mixture of the build plate material and the powder material. The results for the VIS camera are shown in [Figure 5\(b\)](#). Here, the average of 5×5 pixels is shown (corresponding to the same area on the sample as one pixel in the case of the MWIR camera), that is additionally treated by a running average filter of 21 frames to reduce signal fluctuations. Like in the signal of the MWIR camera, the shoulders of melting and solidification can be observed, although the shoulder corresponding to the melting process is less pronounced. Since the data of the MWIR camera is already treated by a camera internal radiometric model, a direct comparison of these results is not possible. To this end, the temperatures for the VIS camera were calculated as follows: We assume a linear response of the camera's detector $I(T)$ to the incident radiance $\Phi_{BB,VIS}(T)$ (calculated by integrating Planck's equation in the spectral window of the band pass filter), i.e.

$$I(T) = c \cdot \Phi_{BB,VIS}(T) \quad (5)$$

We determined the constant c by using the known solidification temperature:

$$c = I(T_{s,2205}) / \Phi_{BB,VIS}(T_{s,2205}) \quad (6)$$

Thus, temperatures T_{cal} that fulfil

$$I(T_{cal}) = c \cdot \Phi_{BB,VIS}(T_{cal}) \quad (7)$$

were used as calibrated temperatures. The results of this calibration are compared to those of the MWIR camera (corrected for the emissivity) in Figure 5(c). Note that the curves were shifted along the time axis to allow for a direct comparison. Except for the cut-off temperature values outside the dynamic range of the VIS camera, the corrected temperature profiles match very well.

3.2. Second experimental run, comparison between MWIR and SWIR cameras

Figure 6(a–d) show thermograms and an intensity image in the case of the uncalibrated SWIR data (in Figure 6(c)) obtained with the MWIR and the SWIR cameras during the build of the ninth layer of the wall. After the application of the described calibration routine assuming a solidification temperature of $T_{s,316L} = 1660$ K for 316 L [1] leading to an emissivity of the solid material of $\epsilon_{316L} = 0.58$ and using data of layer 9, the thermograms of the MWIR and the SWIR camera are very similar (Figure 6(b and d), same colour scale). For quantitative comparison, we have registered both thermograms manually to each other and have calculated the temperature difference (the MWIR thermogram was subtracted from the SWIR thermogram), see Figure 6(e). In addition, we have added a longitudinal profile along this difference image in Figure 6(f). Figure 6(b and d) show

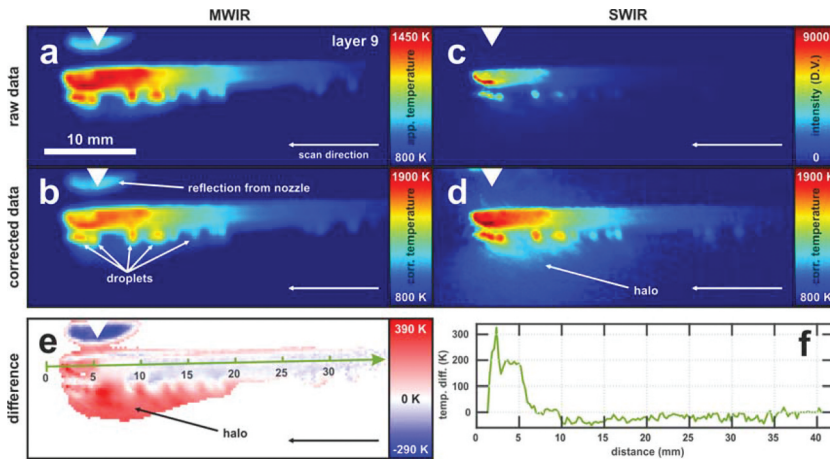


Figure 6. Thermograms recorded during the build of the ninth layer of the wall with the MWIR camera (a and b), intensity image and thermograms recorded with the SWIR camera (c and d) as well as temperature difference image (e) and profile through the difference image (f). The approximate horizontal position of the nozzle is indicated by a triangle. a and c show raw data, b and d show corrected temperature values, obtained by the simple calibration procedure as explained in the text. (a/b): Thermogram at 2.4 s of 3.2 s build duration of the layer. (c/d): Thermogram at 2.4 s of 3.2 s build duration of the layer, d corresponds to a time of 46 s in supplementary video 3. Note that b and d are shown in the same colour scale and are very similar. (e): Difference image between d and b (registration by manual selection of distinct features), limited to the region where both cameras show values within the interval of 800 K to 1900 K. The main difference are the higher corrected temperatures of the SWIR data in the melt pool (see also f) and in the halo below the structure. (f): Profile through e, as indicated.

that the temperature distribution in the cooling tail on the right hand side and the circular structures below the main wall structure are very similar. The circular structures correspond to droplets of solidified material, as comparison to the built structure shows. Observable differences between the thermograms, also shown in [Figure 6\(e\)](#), are: First, similar to [Figure 3\(c\)](#), there is an apparently colder region within the molten pool in the MWIR image ([Figure 6\(b\)](#)). This is not the case for the SWIR image ([Figure 6\(d\)](#)), therefore a positive difference value is shown here in [Figure 6\(e\)](#) and, more apparent, in [Figure 6\(f\)](#). As explained above, this apparent cold spot is most likely caused by a decrease of emissivity in the molten state in the MWIR range and probably an undercooling of the molten state. Apparently, this effect is not present (or reduced) in the SWIR range, since there is no cold spot observable in the molten pool. However, since the real temperature of the molten pool is not known, it cannot be concluded whether the emissivity of the molten pool is reduced compared to the solidified material in the SWIR range. It can only be concluded that a possible intensity drop induced by a reduction of the emissivity of the molten material compared to the solid material is small enough to be at least compensated for by the increase of the temperature of the liquid material. Second, in the area below the wall structure in the SWIR image ([Figure 6\(d\)](#)), there is an extended region with an apparently increased temperature (marked 'halo'), that is not observable in the MWIR image ([Figure 6\(b\)](#)), therefore the difference image shows positive values here ([Figure 6\(e\)](#)). In the data of the first experimental run there are strong signals caused by reflections (see for MWIR, e.g. [Figure 3\(c\)](#)). In that case, the base plate was smooth, leading to a high reflectivity. Here, the used base plate was unpolished (as delivered) to reduce reflections. In addition, this might also be explained by the different observation angles related to the surface normal (60° in the first experimental run, 40° in the second experimental run). At 60° , the reflectivity of metal surfaces usually is higher than at 40° . However, the unpolished plate did not succeed in suppressing reflections in the SWIR range, as observed in [Figure 6\(d\)](#). These reflections are more diffuse than in the MWIR case of [Figure 3\(c\)](#). Since usually the reflectivity of unpolished metals strongly decreases with decreasing wavelength of the light [17,18], this effect cannot be explained by the shorter wavelength of the SWIR camera. Another explanation might be internal reflections within the optical path of the SWIR camera, as here several optical elements are connected to each other (two neutral density filters, one band pass filter and one long pass filter, see [Table 2](#)). Therefore, this effect has to be studied in more detail by adjusting and/or replacing the current optical elements in future experiments. The structures observable in the very top of the images are caused by reflections at the nozzle.

A comparison of the time development of the corrected temperatures during the passing of the laser for the first and the ninth layer formation is shown in [Figure 7\(a\)](#) for the MWIR and the SWIR cameras. First, it is observed that, similar as in the first experimental run, the different cameras show very similar results for the solidified material, especially for times after the solidification plateau. Second, the cooling behaviour for layer 9 is much slower than for layer 1 (e.g. 1350 K/s for layer 9 compared to 4700 K/s for layer 1 at the passing of 1400 K for the MWIR camera), again in accordance with the observations from the first experimental run. In addition, the resting of the temperature values at the solidification point is much longer for layer 9. Third, the MWIR camera shows decreasing corrected temperature values during melting and increasing values during solidification which is similar for both layers. On the one hand side, this can be explained with the lower emissivity

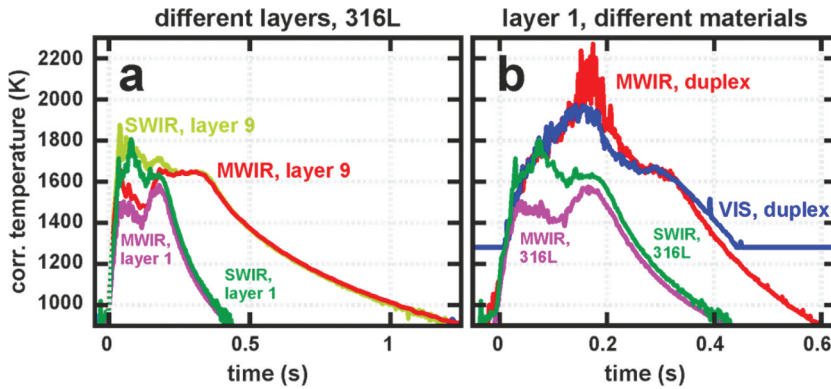


Figure 7. Time evolution of the corrected temperatures at a position that is passed by the laser. The time axes were shifted to match. (a): Data from the second experimental run for layer 1 (same as in b) and layer 9, obtained with MWIR and SWIR cameras. In the cooling tail, SWIR and MWIR cameras show very similar results for the respective layers. The cooling process is much slower for layer 9. (b): Measured data during the build of the first layer of the first experimental run (material: duplex, cameras: MWIR and VIS, same as Figure 5(c)) and the second experimental run (material: 316 L, cameras: MWIR and SWIR). In case of 316 L steel, the differences between the two cameras are larger than in the case of AISI 2205 duplex steel, and the whole heating and cooling process takes less time. This is in accordance with the higher welding velocity, lower beam diameter and lower areal energy density of the 316 L process (compare this in Table 3 above).

of the melt, especially in the MWIR range. On the other hand side, as the temperature seems to be higher after solidification than before melting, it seems that a strong oxidation induced an emissivity increase already for the first layer. This is in accordance with the overall higher emissivity of the solid material of 316 L steel $\epsilon_{316L} = 0.58$ than of AISI 2205 duplex steel $\epsilon_{duplex} = 0.29$, indicating a higher affinity towards oxidation for 316 L steel in accordance with literature [19]. Forth, please note that the data of the ninth layer was used to estimate the emissivity in the MWIR range to adjust the solidification plateau (between 0.25 s and 0.35 s) to the literature value. This emissivity value was used for all layers. For the first layer, the MWIR signal is slightly below the SWIR signal. This is in accordance with the observation that the oxidation (and thus the increase of the emissivity) is lower for the first layer than for following layers, as mentioned above for the first experimental run.

Figure 7(b) shows a comparison of the corrected temperatures during the first layer formation between the first and the second experimental run, thus for different materials and all three camera systems. Besides the already mentioned observations, it is obvious that the whole heating and cooling process takes less time for the second experimental run, which is consistent with the increased welding velocity, decreased laser spot diameter and lower areal energy density (see Table 3). The time in the liquid or mushy state (at the solidification temperature) is much longer in the first experimental run and the cooling rates after solidification are slightly lower (e.g. 3600 K/s in the first experimental run compared to 4700 K/s in the second experimental run at the passing of 1400 K corrected temperature for the MWIR camera). Additionally, it can be observed that the dynamic temperature range of the SWIR camera is similar to that of the MWIR camera, although the temperature noise is strongly increasing for temperatures below 1000 K (standard deviation from a smoothed curve is higher than 20 K at corrected temperatures

below 1000 K compared to below 5 K for temperatures above 1000 K, regarding data from [Figure 7](#) between 850 K and 1350 K in the falling tail). However, the dynamic range of the SWIR camera could be increased by fully using the detector dynamic by increasing the integration time or reducing the neutral density filters. The detector signal was only approximately half saturated for the highest intensities in the current study (9000 D. V. in [Figure 6\(c\)](#) with a saturation at 2^{14} D.V. = 16,384 D.V.). It should also be noted that the temperature dynamic of the MWIR camera would be much higher (considering also lower temperatures) if higher noise levels would have been accepted. The standard deviation from a smoothed curve is below 5 K at all temperatures in the above mentioned data for the MWIR camera. The calibration range by the manufacturer is chosen in such a way that the noise equivalent temperature difference (NETD) is optimum in the whole selected calibration range from 500 K to 1200 K with an integration time of 47 μ s. An extension of the temperature calibration to lower temperatures at this integration time would increase the noise at lower temperatures, but this noise would be acceptable if further information about the temperature distribution is still gained. The curve of the VIS camera showed no significant improvements against the SWIR camera, but has a reduced temperature range at lower temperatures.

4. Conclusion

The performed investigations clearly show the advantages and disadvantages of the three different camera systems with different spectral ranges (MWIR, SWIR, VIS) for process monitoring during the LMD process. The main results are summarised in [Table 4](#).

Although the VIS camera has the best temporal and spatial resolution, there are two main further differences between the results of the MWIR and the VIS camera. Firstly, the

Table 4. Overview of specifications and of observations made with the three different cameras.

	VIS	SWIR	MWIR
Temporal resolution in ms	0.1	2	1.25 to 10
Spatial resolution in μ m	48	125	240 to 260
Length of build wall structure (AISI 2205, first exp. run) in mm	25		45
Length of build wall structure (316 L, second exp. run) in mm		70	70
Temperature range (corr. Temperature) in K at AISI 2205 with $\epsilon = 0.29$ (first exp. run)	1300 to 2000	-	800 to 2300
Temperature range (corr. Temperature) in K at 316 L with $\epsilon = 0.58$ (second exp. run)	-	635 to 2200 (900 to 2200 usable due to noise)	850 to 1750
Reflections of the current weld at the smooth build plate recorded with the camera at 60° to surface normal (first exp. run)	None	-	Several
Reflections of the current weld at the rough build plate recorded with the camera oriented 40° to the surface normal (second exp. run)	-	Several, but very weak and superimposed with high noise at temperatures below 1000 K	Few
Emissivity variations at the wavelength of the camera at the different material states along the melt pool	Lower	Lower	Higher
Observed rim with higher temperature around the melt pool	Fully	visible at layer 3	Partially and fully visible at layer 9
Partially visible at layer 3, partially and fully visible at layer 9			

limited dynamic temperature range of the VIS camera might not be sufficient for process monitoring purposes, if cooling rates and temperature gradients at lower temperatures than 1300 K need to be analysed. Contrary, the dynamic range of the MWIR camera leads to a large measurable temperature range, which might be even enhanced with optimised calibration ranges. The second difference concerns disturbances due to variations of the emissivity and due to reflections. Both, the emissivity and the reflection coefficient, depend on the wavelength. The second local maximum that appears in the MWIR image in [Figure 4\(a\)](#) is not observable in the VIS camera image ([Figure 4\(b\)](#)), indicating lower emissivity variations of the different material states in the case of the VIS camera. Additional experiments at a larger number of layers for the VIS camera will clarify this issue, since in this case the emissivity variations appear to be strongly enhanced for the MWIR cameras results ([Figure 3\(c\)](#)). In addition, reflections from metal surfaces (e.g. the build plate) can only be detected by the MWIR camera, as can be seen in the absence of reflections in the VIS data in [Figure 4\(c\)](#).

The comparison of the MWIR and SWIR cameras in the second experimental run shows that the thermograms of both cameras provide very similar information. The dynamic temperature ranges of both cameras appear to be similar, although the noise of the signal of the SWIR temperature is strongly increasing below 1000 K. The main difference between both cameras is again related to variations of emissivity at different aggregate conditions of the materials: The thermograms and the temporal temperature profiles recorded with the MWIR camera at a fixed position where the laser spot is passing clearly show a decrease of the apparent temperature in the molten state, which is not observable with the SWIR camera. This might be explained with a lower emissivity of the melt pool within the spectral range of the MWIR camera. But as the real temperature of the melt pool is not known, this is only an assumption. A further difference is that although the base plate was unpolished, reflections of the current weld at the base plate are observed with the SWIR camera, while these are not recorded with the MWIR camera. This effect can neither be explained by the different observation angles of the cameras related to the surface normal of the two different experimental runs nor by the wavelength dependences of the reflectivity. As in the second experimental run the observation angle relative to the surface normal was smaller, the reflection should be even lower than in the first experimental run. As mentioned above, reflections within the optical path of the SWIR camera might explain the observations, which will be examined in the future.

Therefore, we conclude that the SWIR as well as the MWIR camera are more suitable to monitor the temporal and spatial temperature changes during the LMD process than the VIS camera. Although the VIS camera has the highest spatial and temporal resolution and has the advantage that reflections from the base plate cannot be detected, its measurable temperature range is not large enough, while the dynamic of the measurable temperature ranges of the SWIR and MWIR camera might be even enhanced by optimal selection of attenuation filters (neutral density filters) and integration time. Here, an optimisation of the optical path of the SWIR camera might even reduce or avoid disturbing reflections. As the SWIR camera is much smaller (and cheaper) and therefore can be more easily integrated into the build space than the MWIR camera, we currently suggest preferring the application of a SWIR camera. A final decision on the selection of one or even more cameras with different specifications should always depend on the specific issues to be addressed.

In addition to information about the selection of appropriate cameras for in-situ monitoring during the LMD process, the study clearly demonstrates that the emissivity (and thus

the reflectivity) of the surface strongly depends on the material state (solid, liquid, oxidised, roughness) and on the wavelength. It has to be considered that the emissivity depends on temperature and observation angle as well. Therefore, a temperature calibration as performed in the study herein by using the known solidification temperature of the materials is only a very rough estimation and is not sufficient for using these temperature evolution values in numerical simulations and/or in predictions about material parameters. As the emissivity depends on that many parameters, it might be very time and resource consuming to experimentally determine all emissivity values for all parameters and all materials. Instead, to predict the almost real temperature evolution, supervised training of an artificial neural network should be possible, using a priori knowledge about the emissivity together with multispectral temporally resolved imaging data of the build process.

If the real temperature evolution is known, this still does not provide direct information about the presence of defects and inhomogeneities. Deviations from simulated or expected temperature distributions might be a hint to a higher probability of the occurrence of defects, but additional information about defects and inhomogeneities, micromechanical structures and mechanical properties of the build structure is needed. This information can be used as input parameters for a supervised training of an artificial neural network as well. Finally, the quality of the build part might be deduced from these almost real temperature dynamics gained from in-situ monitoring of multispectral and/or broadband imaging of the emitted thermal radiation.

Note

1. Note that parts of the presented work regarding the comparison between MWIR- and VIS-camera have previously been published as conference proceedings [10].

Acknowledgments

This research was funded by BAM within the focus area Material.

Disclosure statement

No potential conflict of interest was reported by the authors.

Notes on contributors

Simon J. Altenburg graduated in physics at the Christian-Albrechts-Universität zu Kiel, Germany, in 2009 and conducted his PhD studies there in the field of solid state physics and surface science, graduating in 2014. Since 2015, he works in the department 8.7: Thermographic Methods at BAM. Currently, he is a junior scientist, focusing on thermographic process monitoring in additive manufacturing.

Christiane Maierhofer is a physicist and made her PhD with the focus on solid state physics and surface sciences in 1992 at the Technical University of Berlin. She is head of BAM Division 8.7 Thermographic Methods and has more than 25 year of experience on non-destructive testing, development of active thermography systems, application and coordination of research projects and on standardization.

Andrey Gumenyuk graduated at Tomsk State University (Russia) in the field of physics of metals in 1994, made a postgraduate study and had an assistant position at Technical University St. Petersburg until 1997, worked as research assistant at ISF Welding and Joining Institute RWTH-Aachen University since 1998, where he obtained a PhD degree in Mechanical Engineering in 2004. Since 2007 he is the leader of a scientific group in the field of laser and hybrid welding at BAM.

Anne StraÙe studied engineering at the Technical University in Berlin, Germany. Since 2018 she works at BAM in department 9.3: Welding Technology as research assistant and strives to obtain her PhD degree. In her studies she focuses on in-situ monitoring of Laser Metal Deposition processes.

ORCID

Simon J. Altenburg  <http://orcid.org/0000-0001-6037-4037>

Anne StraÙe  <http://orcid.org/0000-0002-4377-0369>

Andrey Gumenyuk  <http://orcid.org/0000-0002-8420-5964>

Christiane Maierhofer  <http://orcid.org/0000-0003-2398-7170>

References

- [1] DebRoy T, Wei HL, Zuback JS, et al. Additive manufacturing of metallic components – process, structure and properties. *Pro Mater Sci.* 2018;92:112–224.
- [2] Grasso M, Colosimo BM. Process defects and in situ monitoring methods in metal powder bed fusion: A review. *Meas Sci Technol.* 2017;28(4):044005.
- [3] Shamsaei N, Yadollahi A, Bian L, et al. An overview of direct laser deposition for additive manufacturing; part ii: mechanical behavior, process parameter optimization and control. *Addit Manuf.* 2015;8:12–35.
- [4] Yuan K, Guo W, Li P, et al. Influence of process parameters and heat treatments on the microstructures and dynamic mechanical behaviors of inconel 718 superalloy manufactured by laser metal deposition. *Mater Sci Eng A.* 2018;721:215–225.
- [5] Thompson SM, Bian L, Shamsaei N, et al. An overview of direct laser deposition for additive manufacturing; part i: transport phenomena, modeling and diagnostics. *Addit Manuf.* 2015;8:36–62.
- [6] Wargulski DR, Nowak T, Thiele M, et al. Quality management of laser cladding processes for additive manufacturing by new methods of visualisation and evaluation of thermographic data. *Quant Infrared Thermogr J.* 2019;1–12. DOI:10.1080/17686733.2019.1592392
- [7] Griffith ML, Schlienger ME, Harwell LD, et al. Understanding thermal behavior in the lens process. *Mater Des.* 1999;20(2):107–113.
- [8] Schöpp H, Sperl A, Kozakov R, et al. Temperature and emissivity determination of liquid steel s235. *J Phys D Appl Phys.* 2012;45(23):235203.
- [9] Yadroitsev I, Krakhmalev P, Yadroitsava I. Selective laser melting of ti6al4v alloy for biomedical applications: temperature monitoring and microstructural evolution. *J Alloys Compd.* 2014;583:404–409.
- [10] Hofmeister W, Griffith M, Ensz M, et al. Solidification in direct metal deposition by lens processing. *Jom-J Miner Met Mater Soc.* 2001;53(9):30–34.
- [11] Doubenskaia M, Pavlov M, Grigoriev S, et al. Definition of brightness temperature and restoration of true temperature in laser cladding using infrared camera. *Surf Coat Technol.* 2013;220:244–247.
- [12] Eo D-R, Park S-H, Cho J-W. Inclusion evolution in additive manufactured 316l stainless steel by laser metal deposition process. *Mater Des.* 2018;155:212–219.
- [13] Lison M, Devesse W, de Baere D, et al. Hyperspectral and thermal temperature estimation during laser cladding. *J Laser Appl.* 2019;31(2):9.
- [14] Gillespie AR, Rokugawa S, Hook SJ, et al., Temperature/emissivity separation algorithm theoretical basis document, version 2.4. 1999. ATBD contract NAS5-31372, NASA.

- [15] Lane B, Moylan S, Whitenton EP, et al. Thermographic measurements of the commercial laser powder bed fusion process at nist. *Rapid Prototyping J.* **2016**;22(5):778–787.
- [16] Palmer TA, Elmer JW, Babu SS. Observations of ferrite/austenite transformations in the heat affected zone of 2205 duplex stainless steel spot welds using time resolved x-ray diffraction. *Mater Sci Eng A.* **2004**;374(1):307–321.
- [17] Hagen E, Rubens H. Über beziehungen des reflexions- und emissionsvermögens der metalle zu ihrem elektrischen leitvermögen. *Ann Phys.* **1903**;316(8):873–901.
- [18] Spisz EW, Weigand AJ, Bowman RL, et al., Solar absorptances and spectral reflectances of 12 metals for temperatures ranging from 300 to 500 k, in technical note. Washington D. C., USA: National Aeronautics and Space Administration NASA; **1969**. p. 1–21. [cited 2020 February 13]. <https://ntrs.nasa.gov/archive/nasa/casi.ntrs.nasa.gov/19690022517.pdf>
- [19] Fredriksson W, Petrini D, Edström K, et al. Corrosion resistances and passivation of powder metallurgical and conventionally cast 316l and 2205 stainless steels. *Corros Sci.* **2013**;67:268–280.